Supplementary Material

DNA-assisted oligomerization of pore-forming toxin monomers into precisely-controlled protein channels

Anja Henning-Knechtel[1*], Johann Knechtel[2] and Mazin Magzoub[1*]

[1]Biology Program, Division of Science, New York University Abu Dhabi, PO Box 129188, Saadiyat Island Campus, Abu Dhabi, UAE
[2]Department of Engineering, New York University Abu Dhabi, PO Box 129188, Saadiyat Island Campus, Abu Dhabi, UAE

List of Supplementary Items

Supplementary Materials

Section 1| Sequences used for the DNA circle assembly

Supplementary Table 1| List of DNA sequences used for the assembly of the circular DNA scaffolds. P and NH_2 indicate a 5’ phosphorylation and a 5' aminolink C6, respectively.

Name	Sequence (5’ to 3’)
OC01	P-TTTTTGCCGTATTTTTCCTCGCTTTTTCCTCGCTTTTTCCTCGCTT TTTCCTCGCTTTTTCCTCGCTTTTTCCTCGCTTTTTGCCGTA
OC02	P-TTTTTCTCGCTTTTTTCCTCGCTTTTTCCTCGCTTTTTCCTCGCTT TTTCCTCGCTTTTTCCTCGCTTTTTCCTCGCTTTTTCTCGCT
OC03	P-TTTTTGGTGGGTTTTTCCTCGCTTTTTCCTCGCTTTTTGGTGGG
OC04	P-TTTTTTCCTCCTTTTTACCCCTTTTTCCTCGCTTTTTACCCCTTTT TCCTCGCTTTTTACCCCTTTTTCCTCGCTTTTTCACCC
OC05	P-TTTTTCCACTCTTTTTACCCCTTTTTCCTCGCTTTTTACCCCTTTT TCCTCGCTTTTTACCCCTTTTTCCTCGCTTTTTCCCGC
OC06	P-TTTTTCACGTCTTTTTACCCCTTTTTCCTCGCTTTTTCCCCT
OC07	P-TTTTTTCCTCCTTTTTACCCCTTTTTCCTCGCTTTTTACCCCTTTT TCCTCGCTTTTTACCCCTTTTTCCTCGCTTTTTGCCGA
OC08	P-TTTTTAGCCGCTTTTTACCCCTTTTTCCTCGCTTTTTACCCCTTTT TCCTCGCTTTTTACCCCTTTTTCCTCGCTTTTTCACCC
OC09	P-TTTTTCCCACATTTTTACCCCTTTTTCCTCGCTTTTTACCCCTTTT TCCTCGCTTTTTCCCGC
Cap01	ATTGACCCACCAAAAATACGGC
Cap02	AAGTAAGCGAGAAAAACCCACC
Cap03	AGATATACGGCAAAAAAGCGAG
Cap04	ATTGAGGAGGAAAAAAAGGGGAAAAA
Cap05	AAGTAGAGTGGAAAAAGGGTGAAAAA
Cap06	AGATAGACGTGAAAAAGCGGGAAAAA
Cap07	AAGTAGACGTGAAAAAGGGTGAAAAA
Cap08	AGTATGCGGCTAAAAATCGGCAAAAA
Cap09	TATTGTGTGGGAAAAAGGGTGAAAAA
CapComp01	GCCGTATTTTTGGTGGGTCAAT
CapComp02	GGTGGGTTTTTCTCGCTTACTT
CapComp03	CTCGCTTTTTTGCCGTATATCT
CapComp04	TTTTTCCCCTTTTTTTCCTCCTCAAT
CapComp05	TTTTTCACCCTTTTTCCACTCTACTT
CapComp06	TTTTTCCCGCTTTTTCACGTCTATCT
CapComp07	TTTTTCACCCTTTTTCACGTCTACTT
CapComp08	TTTTTGCCGATTTTTAGCCGCATACT
CapComp09	TTTTTCACCCTTTTTCCCACACAATA
IC01a	AAAAAGCGAGTTGTTGTTGTTGAATAA

IC01b	AAAAAGCGAGGTTGTTGTTGTTGAATAA
IC02a	AAAAATACGGTTGTTGTTGTTGAATAA
IC02b	AAAAATACGGCTTGTTGTTGTTGAATAA
IC03a	AAAAAAGCGATTGTTGTTGTTGAATAA
IC03b	AAAAAAGCGAGTTGTTGTTGTTGAATAA
IC04a	AAAAACCCACTTGTTGTTGTTGAATAA
IC04b	AAAAACCCACCTTGTTGTTGTTGAATAA
IC05	AAAAAGGGGTTTGTTGTTGTTGAATAA
IC06a	AAAAAGCGAGGTTGTTGTTGTTGAATAA
IC06b	AAAAAGCGAGTTGTTGTTGTTGAATAA
IC07a	AAAAAGGAGGATTGTTGTTGTTGAATAA
IC07b	AAAAAGGAGGTTGTTGTTGTTGAATAA
IC08	AAAAAGGGTGTTGTTGTTGTTGAATAA
IC09	AAAAAAGGGGTTGTTGTTGTTGAATAA
IC10a	AAAAAGACGTGTTGTTGTTGTTGAATAA
IC10b	AAAAAGACGTTTGTTGTTGTTGAATAA
IC11	AAAAAGCGGGTTGTTGTTGTTGAATAA
IC12a	AAAAAGAGTGGTTGTTGTTGTTGAATAA
IC12b	AAAAAGAGTGTTGTTGTTGTTGAATAA
IC13	AAAAATCGGCTTGTTGTTGTTGAATAA
IC14b	AAAAAGCGGCTTGTTGTTGTTGAATAA
IC15	AAAAAGGGTGTTGTTGTTGTTGAATAA
IC16b	AAAAATGTGGTTGTTGTTGTTGAATAA
ssDNA tail'	NH_2–TTATTCAACAACAA

Supplementary Table 2| Assignment of the sequences for the different DNA templates.

DNA structure	DNA sequence				
	Outer Circle	Cap-L	Cap-C	CapComp	Inner Circle
Icosamer					
$[11^-]_{20}$	OC01, OC02, OC03	Cap01, Cap02	Cap03	CapComp01, CapComp02, CapComp03	IC01b, IC02b, IC03b, IC04b
$[11^+]_{20}$	OC01, OC02, OC03	Cap01, Cap02	Cap03	CapComp01, CapComp02, CapComp03	IC01a, IC02a, IC03a, IC04a
$[21^-]_{20}$	OC04, OC05, OC06	Cap04, Cap05	Cap06	CapComp04, CapComp05, CapComp06	IC05, IC06a, IC07a, IC08, IC09, IC10a, IC11, IC12a
$[21^+]_{20}$	OC04, OC05, OC06	Cap04, Cap05	Cap06	CapComp04, CapComp05, CapComp06	IC05, IC06b, IC07b, IC08, IC09, IC10b, IC11, IC12b
Dodecamer					
$[21^+]_{12}$	OC04, OC06	Cap04	Cap07	CapComp04, CapComp07	IC05, IC06b, IC07b, IC08, IC09, IC10b
Hexacosamer					
$[21^+]_{26}$	OC06, OC07, OC08, OC09	Cap04, Cap08, Cap09	Cap06	CapComp04, CapComp06, CapComp08, CapComp09	IC05, IC06b, IC07b, IC09, IC10b, IC11, IC13, IC14b, IC15, IC16b

Section 2| Additional data for the DNA/αHL hybrid formation

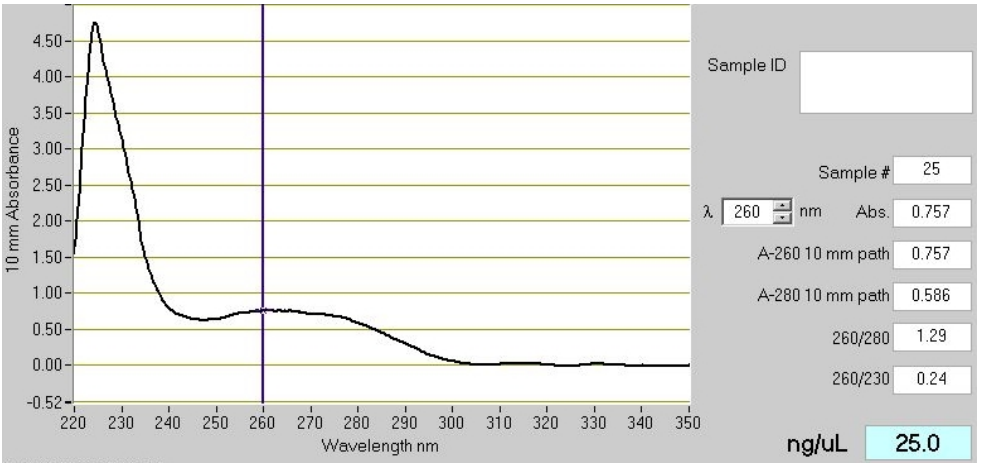

Supplementary Figure 1| Typical 260 and 280 nm absorbance of DNA-modified K237C-αHL mutants using a NanoDrop spectrophotometer. The sample was filtered to remove unbound oligonucleotides. Using an extinction coefficient of $\varepsilon^{1\%} = 11$ (1), the calculated concentration of αHL monomers was 16.1 µM. The calculated DNA concentration of 5.93 µM was determined using the ssDNA-specific conversion factor of 33 µg/OD_{260}. Thus, the ratio of DNA to protein was 1:2.7. Unmodified αHL monomers were removed after the conjugation with the DNA templates. Gel electrophoretic separation of the sample is shown in Figure 1f (lane 3).

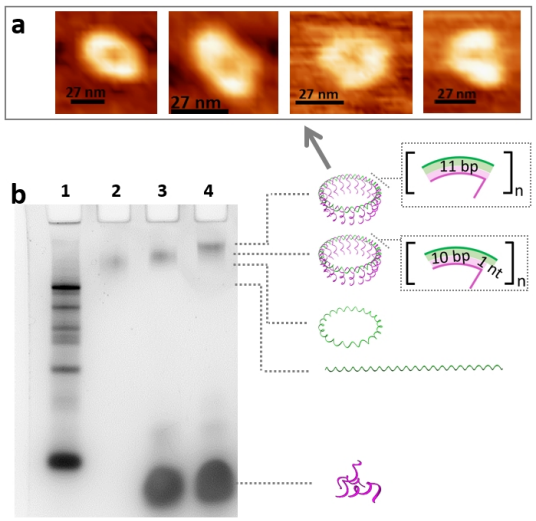

Supplementary Figure 2| 220-bp-DNA template assemblies. a, AFM images of DNA structures based on 11 bp per helical turn. Scale bars = 27 nm. **b**, $MgCl_2$-supplemented native PAGE analysis of 220-bp-DNA template assemblies. Lane 1: ligation of 3 oligonucleotides to the linear ssDNA strand; lane 2: circularized ssDNA strand; lane 3: dsDNA $[11^+]_{20}$-circle; lane 4: dsDNA $[11^-]_{20}$-circle.

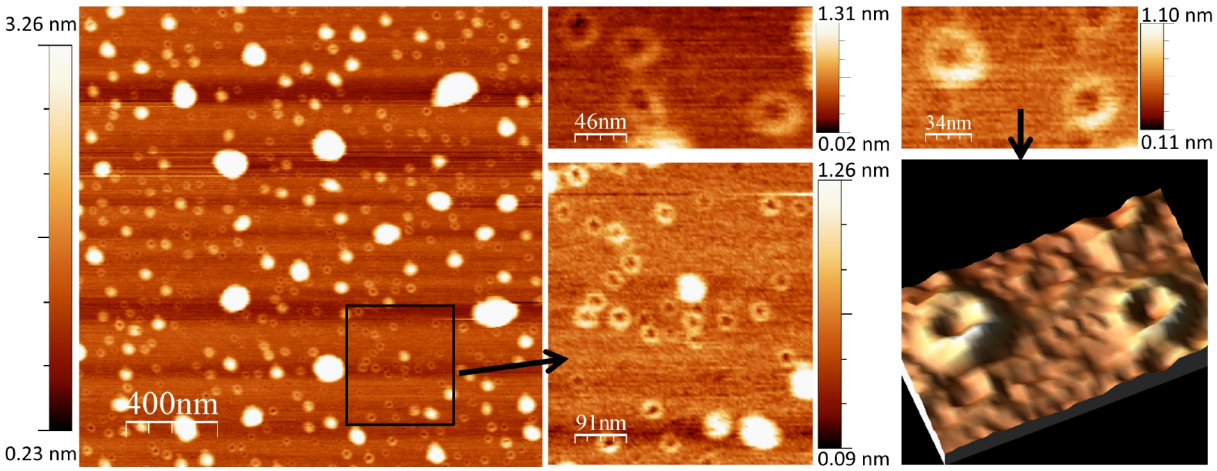

Supplementary Figure 3| AFM topography images of $[21^+]_{20}$-DNA nanostructures. Additional AFM images of the $[21^+]_{20}$-DNA nanostructures without αHL. The images show a homogenous distribution of the DNA nanostructures.

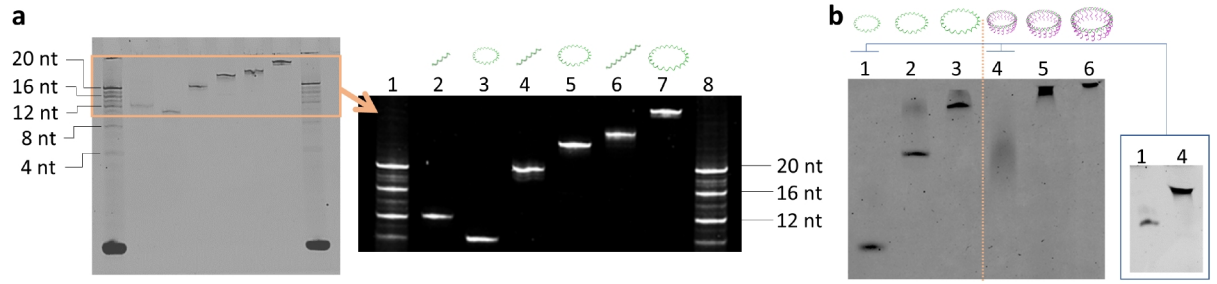

Supplementary Figure 4| Native PAGE analysis of $[21^+]_{12}$-, $[21^+]_{20}$-, and $[21^+]_{26}$-DNA assemblies. a, Comparison of linear and circularized ssDNA scaffold strands with 12, 20, and 26 domains. Lanes 1 and 8: ligation of 3 oligonucleotides to the linear 210-nt long ssDNA strand; lane 2: linear 126-nt ssDNA long strand; lane 3: circularized 126-nt long ssDNA strand; lane 4: linear 210-nt long ssDNA; lane 5: circularized 210-nt long ssDNA; lane 6: linear 273-nt long ssDNA; lane 5: circularized 273-nt long ssDNA. Note that the circular ssDNA strand with 12 segments (lane 3) runs before the linear strand since its compact shape enables it to pass the pores of the gel more easily. The two gels represent 10% PAGE gels that were run under the same conditions, but for different durations. **b**, Comparison of single-stranded and double-stranded circular $[21^+]_j$-DNA templates. Lane 1: circularized 126-nt long ssDNA strand; lane 2: circularized 210-nt long ssDNA; lane 3: circularized 273-nt long ssDNA; lane 4: circularized 126-nt long dsDNA strand; lane 5: circularized 210-nt long dsDNA; lane 6: circularized 273-nt long dsDNA. The $[21^+]_{12}$-DNA structure runs in a 10% PAGE gel (supplemented with 6 mM $MgCl_2$) as a smear; running it in a 15%-Mg^{2+} PAGE gel results in a sharp band with a lower mobility than the 126-nt long ssDNA scaffold, as shown in the inset.

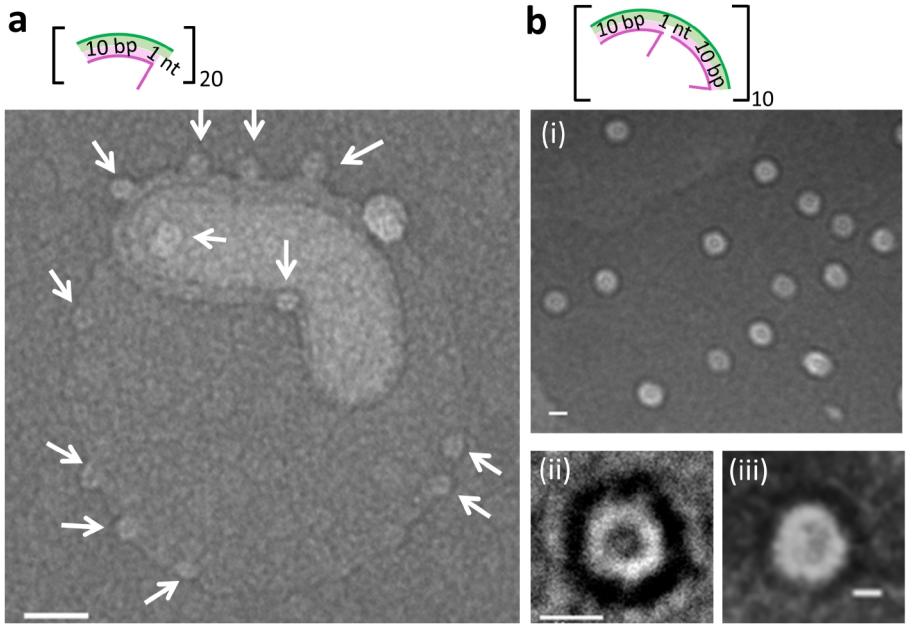

Supplementary Figure 5| TEM micrographs of DNA/αHL icosamers based on a, 11 bp, or b, 10.5 bp, per helical turn in the presence of DPhPC liposomes. Hybrid pores were found mainly adhered to the liposomes or on lipid covered areas. Scale bar: **a**: 50 nm; **b**: (i) 20 nm, (ii) 10 nm, (iii) 10 nm.

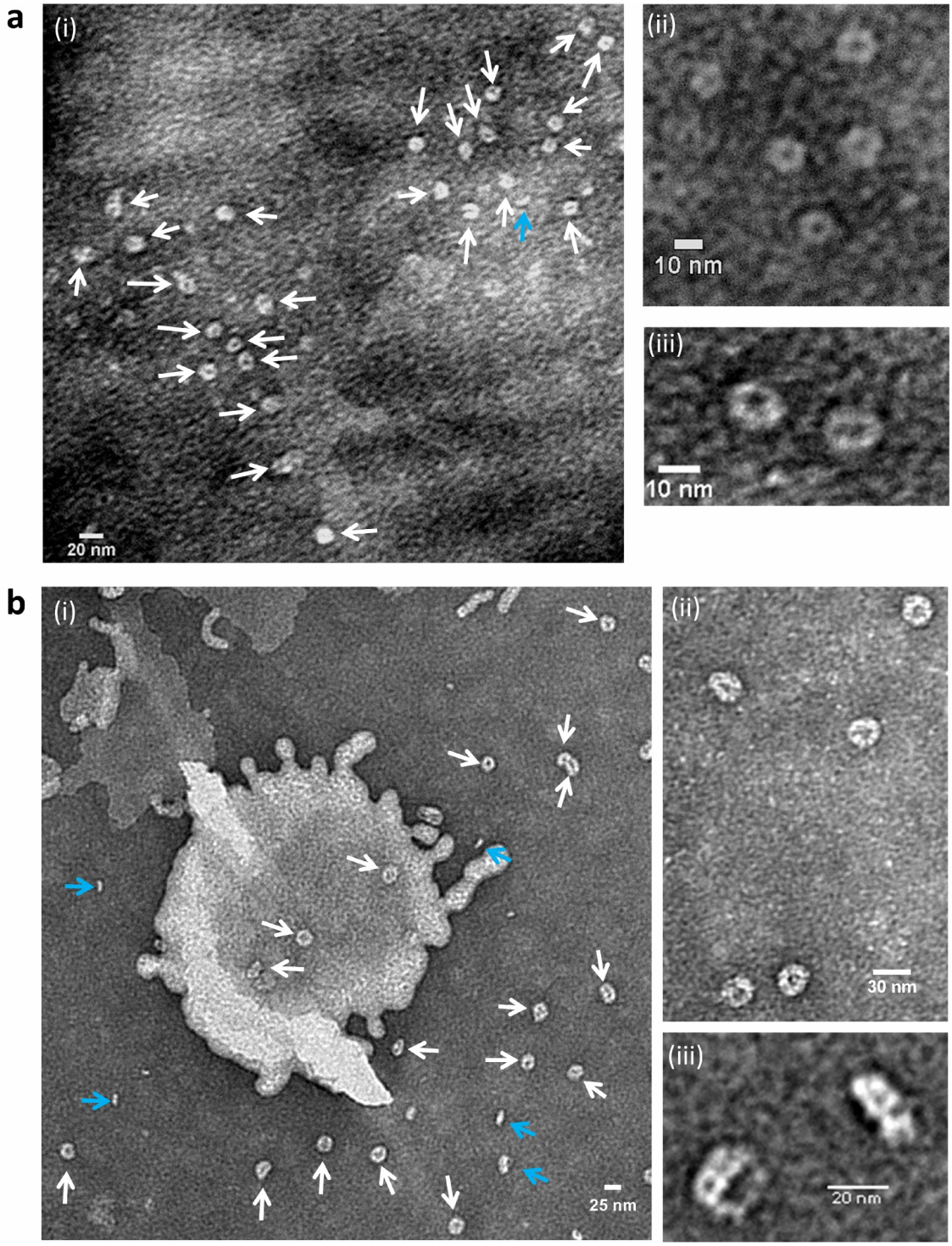

Supplementary Figure 6| TEM micrographs of **a**, DNA/αHL dodecamers, and **b**, hexacosamers, based on 10.5 bp per helical turn in the presence of DPhPC liposomes. It should be noted that the liposomes could potentially be subject to membrane rupturing upon an increasing number of pore insertions, which would result in lipid bilayer fragments on the TEM grid that include the inserted pores. White and blue arrows indicate the plane and side view of DNA/αHL hybrid pores, respectively.

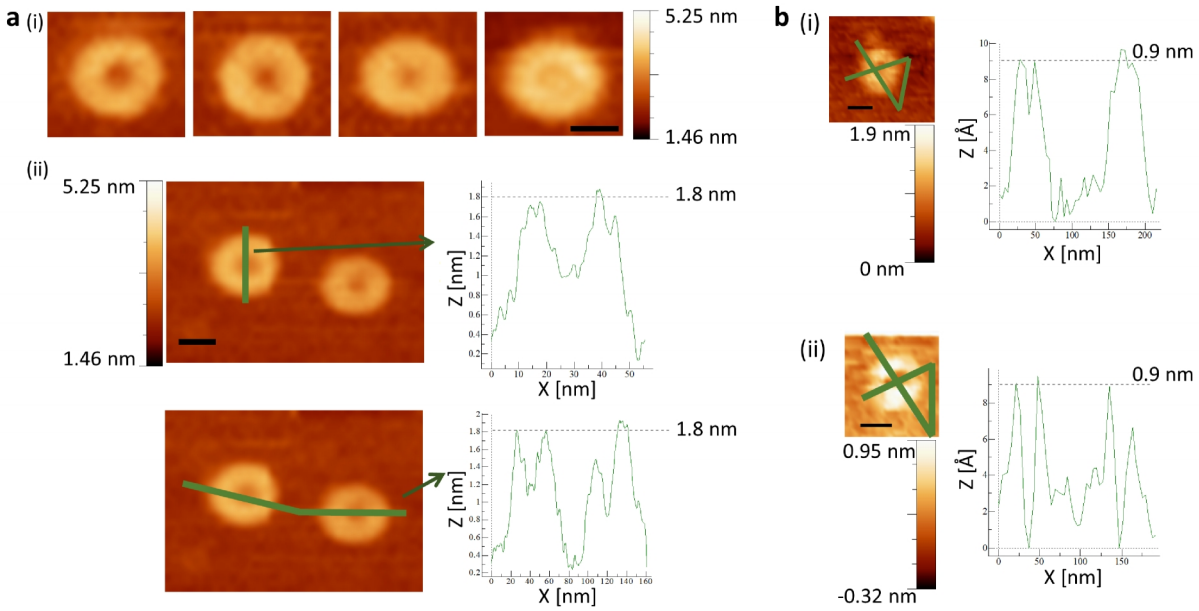

Supplementary Figure 7| AFM images of $[21^{+}]_{20}$-DNA templates with (**a**) and without (**b**) αHL monomers. Scale bar is 27 nm and applies to all images.

Section 3| Single channel recordings of icosameric hybrid constructs based on a DNA circle without free nucleotides

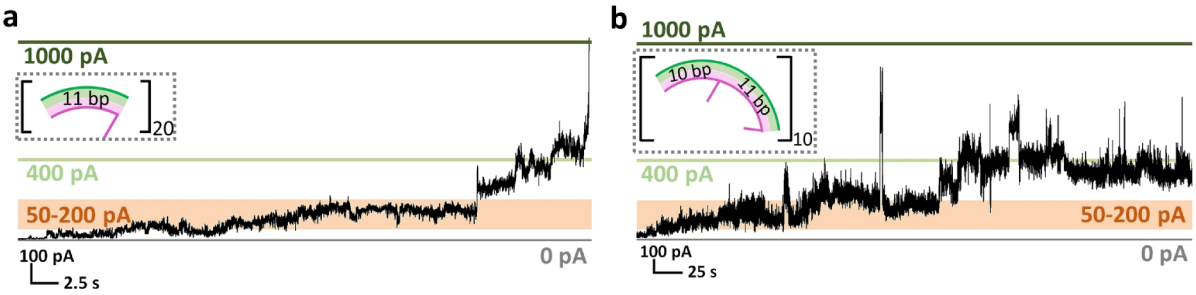

Supplementary Figure 8| Electrical recordings of DNA-templated αHL icosamers without unpaired nucleotides. Typical insertion trace for a hybrid pore containing a double-stranded DNA circle based on either **a**, 11 bp, or **b**, 10.5 bp, per helical turn. Purified DNA/protein hybrid structures were incorporated into DPhPC bilayers in 0.1 M KCl, 25 mM Tris HCl (pH 7.99) with 50 µM EDTA. A potential of 100 mV was applied to the *trans*-side, with the *cis* compartment connected to the ground.

Section 4| Electrical recordings of the DNA and protein components of DNA/αHL hybrid pores

Electrophysiological recordings with DNA-modified K237C mutants resulted in only a few events with an insertion pattern and conductance typical for a heptameric αHL pore (2) (Supplementary Fig. 9a). In experiments where only DNA-templates were added, no lipid-bilayer interactions were observed (Supplementary Fig. 9b).

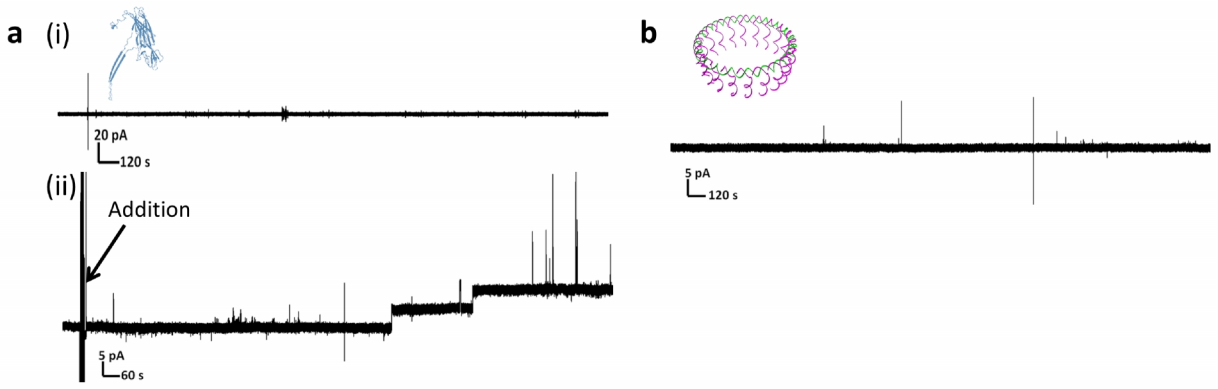

Supplementary Figure 9| **a**, Single channel recordings of DNA-modified K237C-αHL mutants (i) at the same, or (ii) at a 5-fold higher, concentration as used for electrical recordings of the DNA/αHL hybrid structures. **b**, Typical current trace of DNA templates with twenty $[21^{+}]_{j}$-DNA segments at a 5-fold higher concentration than used in DNA/αHL hybrid experiments. Purified proteins (10-kDa MWCO filter device) and DNA structures (30-kDa MWCO filter device) were added to the *cis*-side of a DPhPC bilayer in 0.1 M KCl buffer containing Tris-EDTA. A potential of 100 mV was applied to the *cis*-side of the chamber.

Section 5| Additional electrical recordings of DNA/αHL hybrid pores

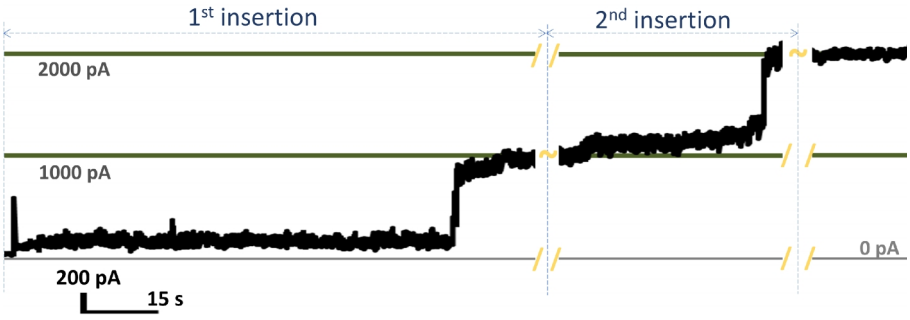

Supplementary Figure 10| Typical trace for multiple channel insertions. $[11^{+}]_{20}$-DNA/αHL hybrid constructs were added to the *cis*-side of the setup. Each hybrid pore formation features the stepwise insertion.

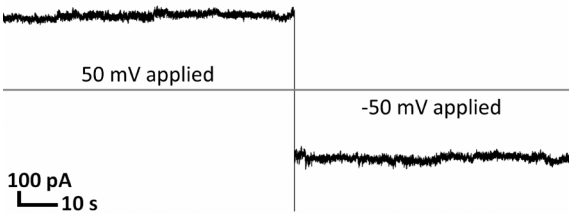

Supplementary Figure 11| Representation of current values at positive and negative potential for an open $[21^{+}]_{20}$-DNA/αHL hybrid pore.

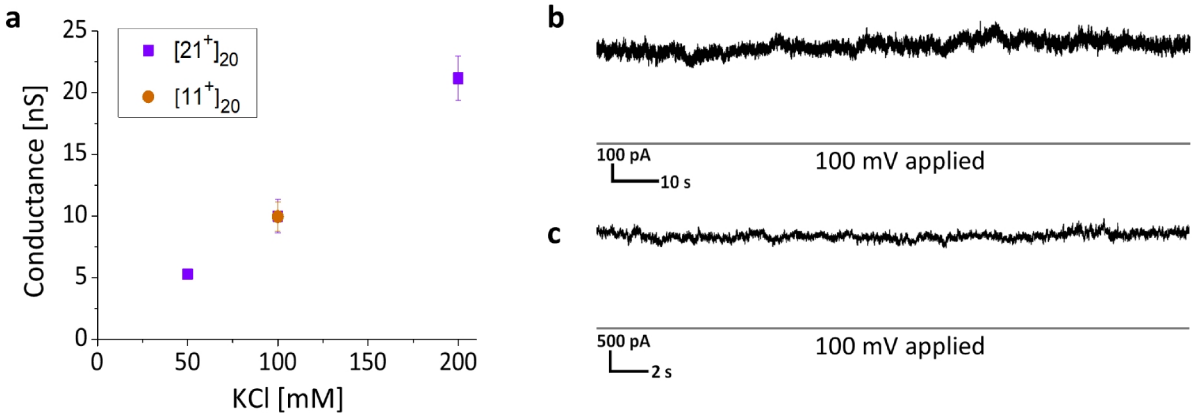

Supplementary Figure 12| a, KCl concentration dependence of the conductance of pores assembled on an unpaired nucleotide-containing icosameric DNA template. Single channel recordings of pores with 10.5 bp/turn-based DNA structures at **b**, 50 mM, and **c**, 200 mM salt concentration. Purified DNA/protein hybrid structures were incorporated into DPhPC bilayers in 25 mM Tris HCl (pH 7.99), with 50 µM EDTA.

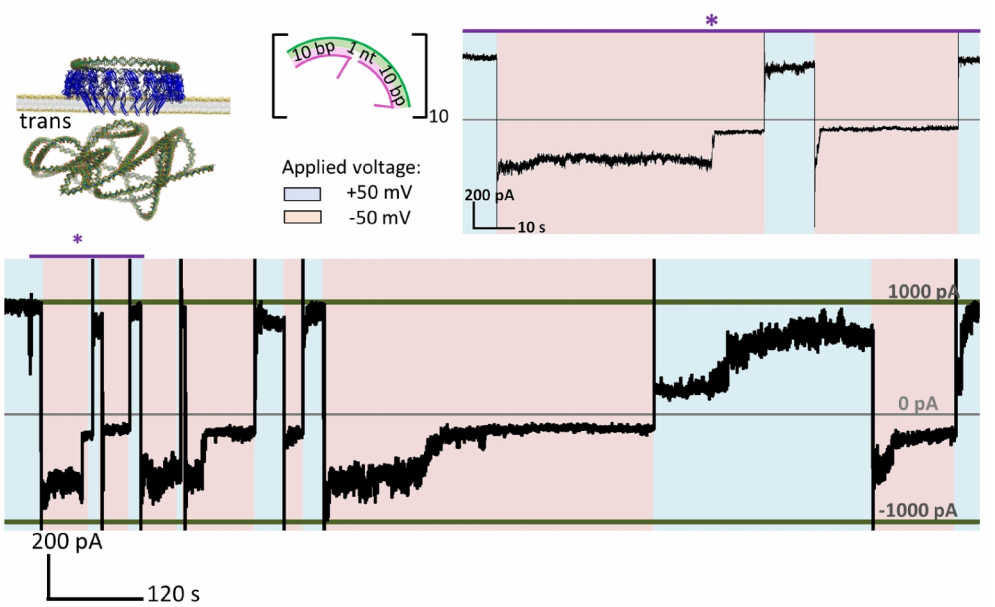

Supplementary Figure 13| Electrical recording of a $[21^{+}]_{20}$-icosameric hybrid pore that is stochastically blocked by the addition of λ-DNA to the *trans*-side. Extended trace of Figure 5b is shown on the upper right-hand side.

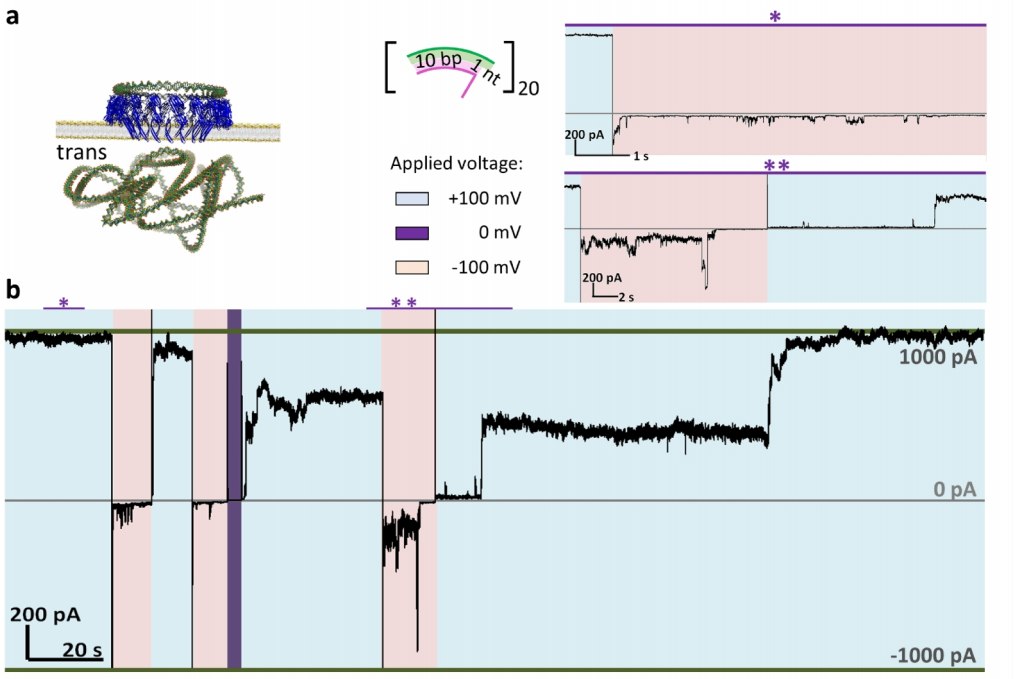

Supplementary Figure 14| Blockage of a homo-icosameric αHL pore. a, λ-DNA molecules were added to the *trans*-side after a purified DNA/αHL hybrid structure was incorporated into a DPhPC bilayer. **b**, Electrical recording of an icosameric hybrid pore based on $[11^{+}]_{j}$-DNA segments at applied positive (+100 mV; shaded in blue) and negative (-100 mV; shaded in red) potential. Magnified sections of the trace (*,**) are shown on the upper right-hand side.

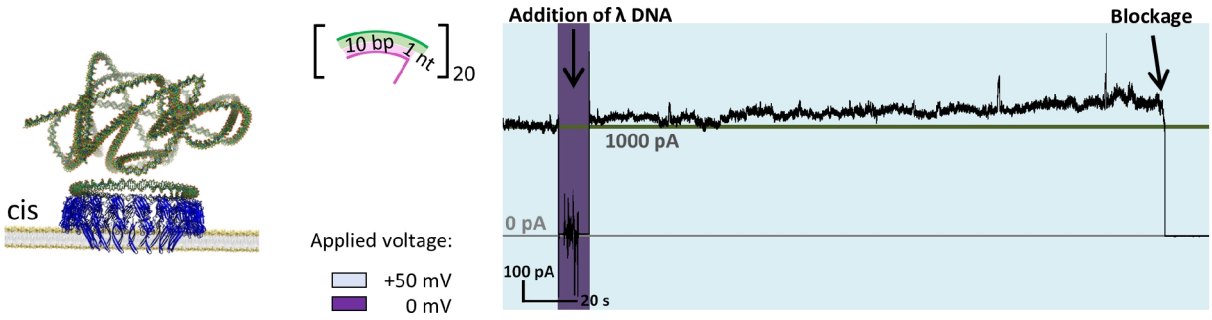

Supplementary Figure 15| Electrical recording of blockage of homo-icosameric αHL pore due to λ-DNA addition to the *cis*-side. 0 mV were applied during the addition of 15.6 fM λ-DNA (shaded in purple). The application of a positive potential (+50 mV; shaded in blue) resulted in a complete blockage of the conductance.

Section 6| Overview of observed conductance and noise in planar lipid bilayer experiments

The open pore conductances and noise in PLB recordings for the different hybrid constructs are summarized in Supplementary Tables 3 and 4, respectively.

Supplementary Table 3| List of the observed open pore conductances for αHL monomers in the presence and absence of a DNA template, during planar lipid bilayer recordings.

Number of connected αHL mono-mers	αHL monomers	DNA template	Conductance in planar lipid bilayer experiments (0.1 M KCl solution)	Number of independent insertions used for conductance determina-tion	Number of independent prepared structures used for conductance determination
12	ssDNA-modified K237C mutant	$[21^+]_{12}$	2.28 ± 0.29 nS	27	3
20	ssDNA-modified K237C mutant	$[11^-]_{20}$	No complete insertion	0	3
20	ssDNA-modified K237C mutant	$[11^+]_{20}$	9.98 ± 1.36 nS	43	5
20	ssDNA-modified	$[21^-]_{20}$	9.98 ± 0.84 nS (before rupture of membrane)	3	3
20	ssDNA-modified K237C mutant	$[21^+]_{20}$	10.16 ± 0.94 nS	53	5
26	ssDNA-modified K237C mutant	$[21^+]_{26}$	25.03 ± 2.76 nS	21	5
1	ssDNA-modified K237C mutant	-	0.07 ± 0.03 nS	18	1
1	wild type	-	0.09 ± 0.01 nS	10	1

Supplementary Table 4| Noise values for αHL monomers in the presence and absence of a DNA template. Electrical recordings were performed in a 0.1 M KCl containing buffer solution. The histograms of 500 ms recordings at +100 mV and 0 mV were Gaussian fitted to calculate the noise values (± standard deviation) according to $((\sigma^{0\ mV})^2 + (\sigma^{+100\ mV})^2)^{1/2}$. Ten independent insertions were averaged for the determination of the mean noise values.

Number of connected αHL monomers	Noise
12 (ssDNA-modified K237C mutant)	9.50 ± 3.02
20 (ssDNA-modified K237C mutant)	22.56 ± 5.75
26 (ssDNA-modified K237C mutant)	25.61 ± 6.18
1 (ssDNA-modified K237C mutant)	2.38 ± 0.46
1 (wild type)	0.40 ± 0.02

Section 7| Modelling the β-hairpin alignment within αHL pores

Here, we present an approach to calculate the dimensions of the β-barrel of an αHL pore that depends on the arrangement of the β-strands in the natural heptamer (3-5). This geometrical model is based on the variation of subunit-subunit interaction between adjacent β-hairpins; the number and nature of intramolecular bonds remain the same, and hence the structure of each domain within the αHL monomers is unchanged. Using this approach, we could design a barrel for the αHL heptamer and obtain values for the pore diameter and height that are in agreement with the dimensions of the crystal structure. In addition, the model was verified with the reconstruction of an additional biological pore, i.e. the *Mycobacterium smegmatis* porin A (MspA) octamer (6). Calculating the theoretical dimensions of a β-barrel that includes 12, 20 or 26 monomers shows that larger numbers of αHL monomers can also form pores with diameters of ~14, 20 or 30 nm, respectively.

αHL_7 in a membrane

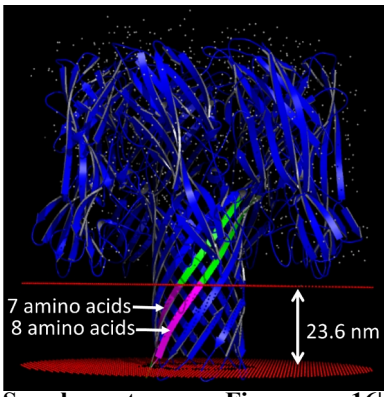

Supplementary Figure 16| Orientation of α-hemolysin in a membrane.

Each protomer within the αHL heptamer (αHL_7) consists of 293 amino acids (aa's) that form an amino latch, β-sandwich domain, triangle region, stem domain and rim domain (7). The stem region forms the anti-parallel β-sheet barrel of the αHL_7 and is composed of two β-strands (residues E111–K147) that are separated by a five aa-long turn region. The β-strands are oriented with a 180° twist in a right-handed manner and tilted by 38°.

Supplementary Figure 16 shows the result of a simulation that reveals the orientation of a αHL_7 pore in a membrane (source: Orientation of proteins in membrane (OPM) database). As can be seen, only the lower part of the β-barrel is inserted into the membrane. Out of 16 aa's per β-strand, only 7–8 aa's are involved, corresponding to a β-barrel height 1.98–2.26 nm. Their respective sequences are GFNGNVT and GGLIGANV. In addition, the two β-sheet flanking aa's of the central turn region are localized in the lipid bilayer as well.

Calculation of the dimensions of the β-barrel for a pore of 7, 12, 20 or 26 αHL monomers

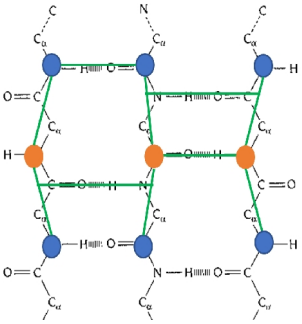

Supplementary Figure 17| Schematic representation of an antiparallel β-sheet showing the alternating positions of hydrogen bonds between the amino acids.

A β-strand – within any antiparallel β-sheet – is naturally arranged as a series of two aa's that alternately form two hydrogen bonds with the β-strand either to their left or to their right (Supplementary Fig. 17). This implies that β-strands can be offset against each other by a distance of 2 aa's in order to allow for the formation of hydrogen bonds between both strands.

Considering the N- and C-strand of one αHL β-hairpin without the central turn region as one common β-strand unit will permit the offsetting shifts to cover 2, 4, 6, 8, 10, 12 or 14 aa's between them. Supplementary Figure 18 shows, as an example, the shift of two aa's per β-strand units within a sheet that is composed of three β-strand units. Thereafter, the orientation of the sheet in a two-dimensional (2D) space needs to be corrected such that the "mushroom parts" of the αHL monomer are linearly aligned.

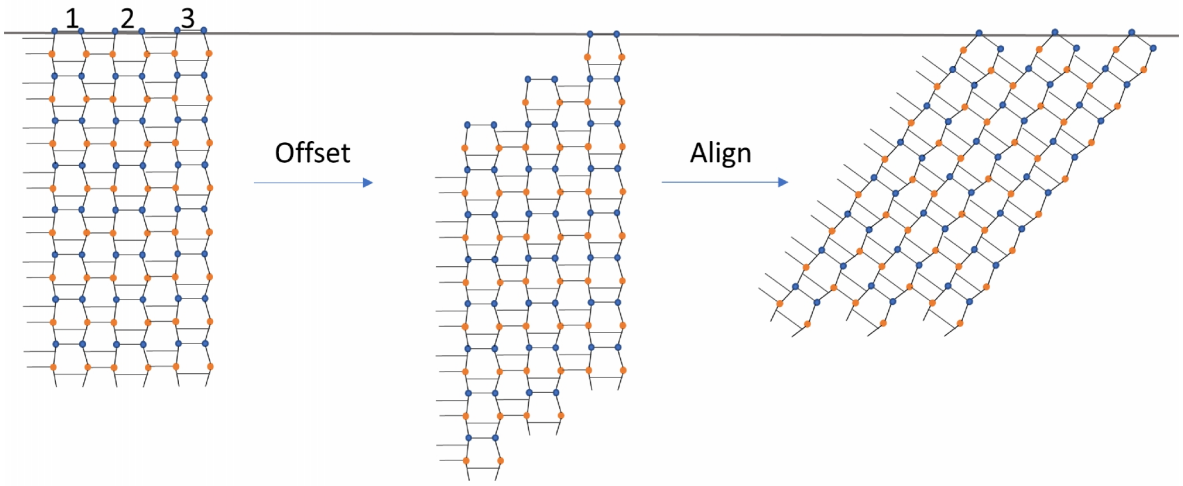

Supplementary Figure 18| Schematic representation of the β-strand unit alignment within an antiparallel β-sheet.

The resulting 2D sheet can be conceptually rolled up into a cylinder. The diameter, *d*, of the cylinder can be calculated as follows:

$$d = \frac{N * \sqrt{a^2+b^2}}{\pi}; \qquad \text{(S1)}$$

where *N* represents the number of monomers, *a* the distance between the β-strand units, and *b* the length of the offset (Supplementary Fig. 19). For *a* and *b*, 0.92 nm and 0.36 nm/aa can be considered, respectively.

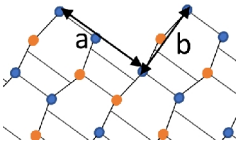

Supplementary Figure 19| Schematic representation of the distances within a rearranged β-sheet that were used to calculate the diameter, *d*, and height, *h*, of the resulting β-barrel.

The height of the β-barrel can be calculated using following equation:

$$h = l_{\text{beta-hairpin}} * \frac{a}{\sqrt{a^2+b^2}}, \qquad \text{(S2)}$$

with $l_{beta\text{-}hairpin}$ representing the length of the β-strand that is involved in the β-sheet formation, e.g. 5.76 nm for 16 aa's.

As an example, a cylinder which comprises seven αHL monomers with an offset of 2 aa's would give a calculated *d* of 2.6 nm and *h* of 4.54 nm. Analysis of the crystal structure of the natural occurring heptamer (Supplementary Fig. 20) indicates that the β-barrel contains a two-aa long shift, and reveals dimensions that are in agreement with the calculated ones (d = 2.6 nm; h = 4.52 nm). A comparison of the crystal with the calculate structures of the β-barrel is given in Supplementary Figure 22.

We further verified the αHL-based model by reconstructing the β-barrel of MspA. This pore is an example of natural β-barrel with a 4-aa offset between eight 12-aa-long β-hairpin units (Supplementary Fig. 21a). The modelled pore diameter and alignment of the β-strand units match the β-barrel of the crystal structure of MspA (Supplementary Fig. 21b).

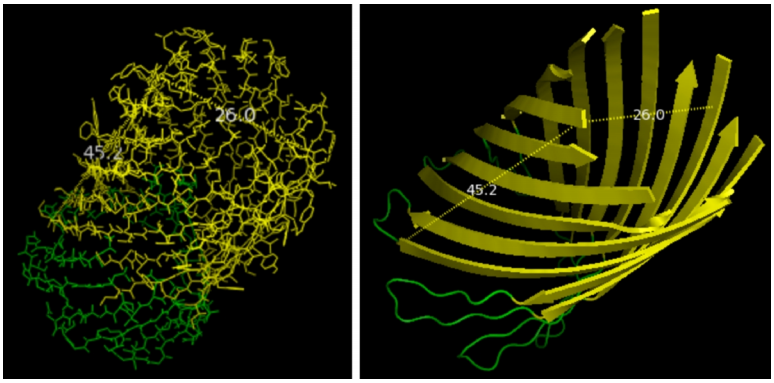

Supplementary Figure 20| Pymol representation of the heptameric α-hemolysin crystal structure (PDB: 7ahl). β-strands and loops are shown in yellow and green, respectively.

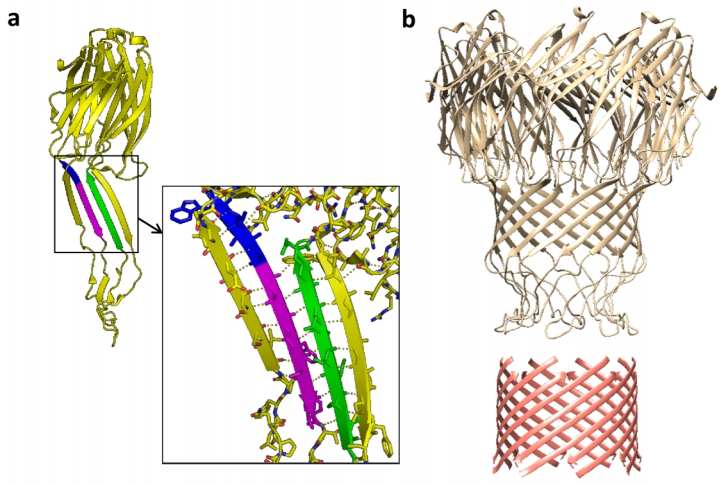

Supplementary Figure 21| MspA as a natural example for a 4-aa offset pore. a, The β-hairpins in MspA are connected with a 4-aa offset. The β-strands that form hydrogen bonds and the offset are highlighted in magenta and blue, respectively. **b**, Comparison of the crystal structure of MspA (gold, PDB:1UUN) with the generated octameric β-barrel with a 4-aa offset (salmon-pink). Note that the model uses α-hemolysin β-strands which are longer than the MspA ones, and thus the modelled MspA β-barrel has a greater height compared to the one in the crystal structure.

We then applied the model to calculate and visualize the height and diameter of a β-barrel that contains 12, 20 or 26 monomers. Using the obtained variables, we could further calculate the conductance as a function of the diameter as described by Kowalczyk *et al.* (8):

$$G = \sigma \left[\frac{4H}{\pi {d_c}^2} + \frac{1}{d_c} \right]^{-1}, \qquad \text{(S3)}$$

where H is the pore height, d_c the pore diameter at its *lys-gln* central constriction (channel diameter minus 1.2 nm), and σ and the electrolyte conductivity. A 0.1 M KCl solution at 25 °C was reported to have a conductivity of 1.28246 S/m (9). The results are summarized in Supplementary Figure 23 and Supplementary Table 5.

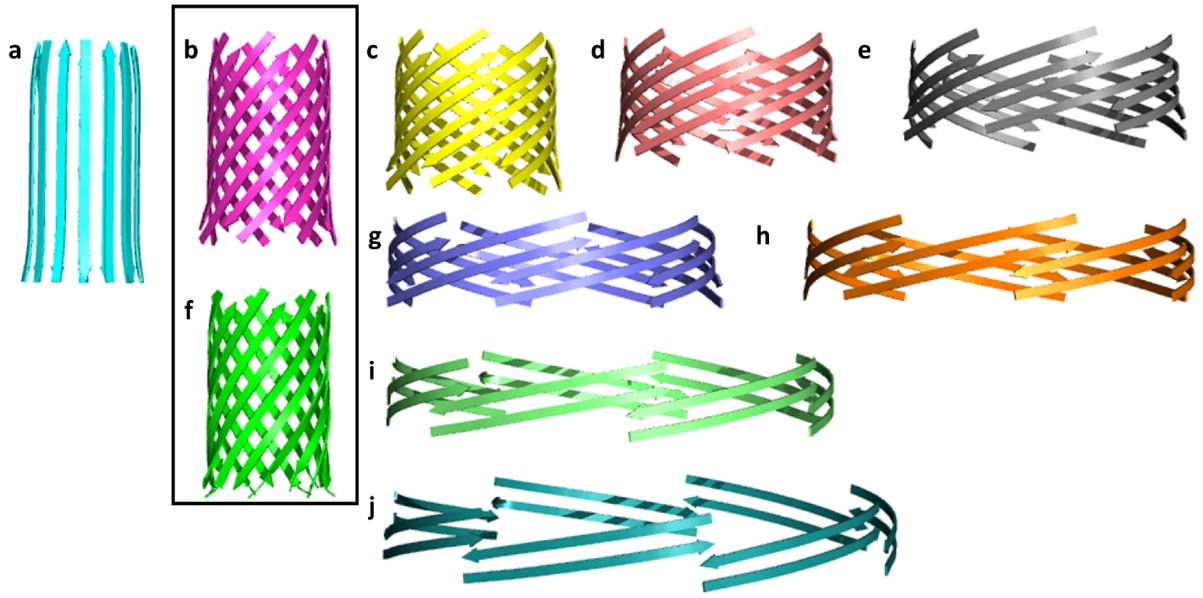

Supplementary Figure 22| Comparison of β-barrels formed by 7 αHL monomers at different amino acid offsets between adjacent monomers. β-barrels were generated with an offset of **a**, 0 aa's; **b**, 2 aa's; **c,** 4 aa's; **d**, 6 aa's; **e**, 8 aa's; **g**, 10 aa's; **h**, 12 aa's; **i**, 14 aa's; **j**, 16 aa's. **f**, Crystal structure of the α-hemolysin β-barrel (PDB code:7aHL).

Supplementary Table 5| Calculated parameters for heptameric, dodecameric, icosameric and hexacosameric αHL pores at different offsets, *S*. *x* represents the distance between the β-hairpins, *h* the height of the β-barrel, *H* the total height of the protein pore, *d* the diameter of the β-barrel and *D* the outer diameter of the protein[1].

				αHL heptamer		αHL dodecamer		αHL icosamer		αHL hexacosamer	
S	x	h	H	d	D	d	D	d	D	d	D
[AA]	[nm]	[nm]	[nm]	[nm]	[nm]	[nm]	[nm]	[nm]	[nm]	[nm]	[nm]
0	0.92	5.76	11.22	2.05	9.28	3.51	11.26	5.86	13.60	7.61	15.36
2	1.17	4.54	10.00	2.60	9.83	4.46	12.21	7.44	15.18	9.67	17.41
4	1.71	3.10	8.57	3.81	11.04	6.53	14.27	10.88	18.62	14.14	21.89
6	2.35	2.26	7.72	5.23	12.46	8.97	16.71	14.95	22.69	19.43	27.17
8	3.02	1.75	7.22	6.74	13.97	11.55	19.29	19.25	26.99	25.02	32.77
10	3.72	1.43	6.89	8.28	15.51	14.19	21.94	23.65	31.40	30.75	38.50
12	4.42	1.20	6.66	9.84	17.07	16.87	24.61	28.12	35.86	36.55	44.30
14	5.12	1.03	6.50	11.42	18.65	19.57	27.31	32.62	40.36	42.40	50.14
16	5.83	0.91	6.37	13.00	20.23	22.28	30.02	37.13	44.88	48.27	56.02

[1] The outer diameter was calculated as follow: D = d + x; where x is 7.23 nm or 7.74 nm for an odd or even number of monomers, respectively.

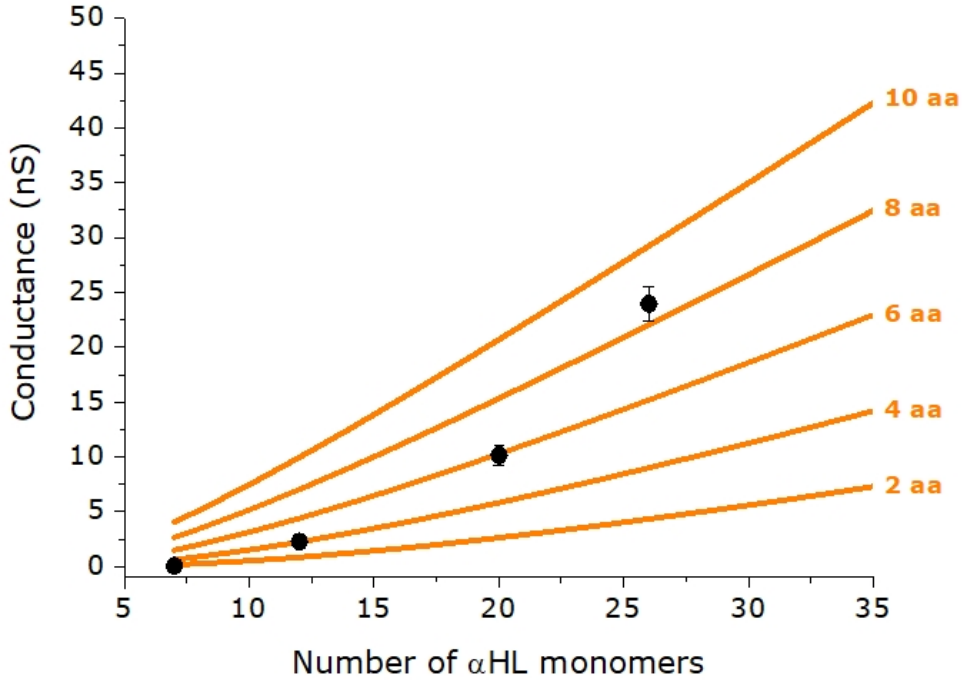

Supplementary Figure 23| Comparison of the experimental and β-barrel based-modelling (see above) obtained conductance for DNA/αHL hybrid pores. The orange lines indicate the theoretical conductance values of the pore versus the number of αHL monomers for β-barrels with an offset of 2, 4, 5, 8 or 10 aa's. The experimental data are shown as black circles.

Supplementary Figure 23 illustrates the conductance as a function of the number of αHL monomers in the hybrid pore. The theoretical curves (orange) are based on an hourglass-like model for the pore's shape (8); however, that model may reflect the underlying alpha-hemolysin's shape only to some extent. Taking this and the experimental error into account, the experimental data is well within the range of the theoretical values along the different aa-offset-curves. A comparison between the experimental and theoretical values indicates larger offset lengths for an increasing number of monomers. This is expected, as the offset will naturally adjust along with the number of monomers (to compensate for increasing β-hairpin distances) towards the energetically most favourable barrel formation. In turn, this results in alterations for both the pore diameter and height. Consequently, the conductance-monomer correlation is expected to scale stepwise and linearly. The largest possible β-hairpin distances can be compensated for by a 10-aa-offset-based β-barrel. This implies that the conductance for pores comprising more than ~26 monomers depends mainly on the diameter of the pore; the conductance of such large pores can accordingly be derived from the 10-aa-offset curve. Moreover, the height in this regime is expected to remain constant at ~6.89 nm.

Section 8| Formation of the αHL pore cap

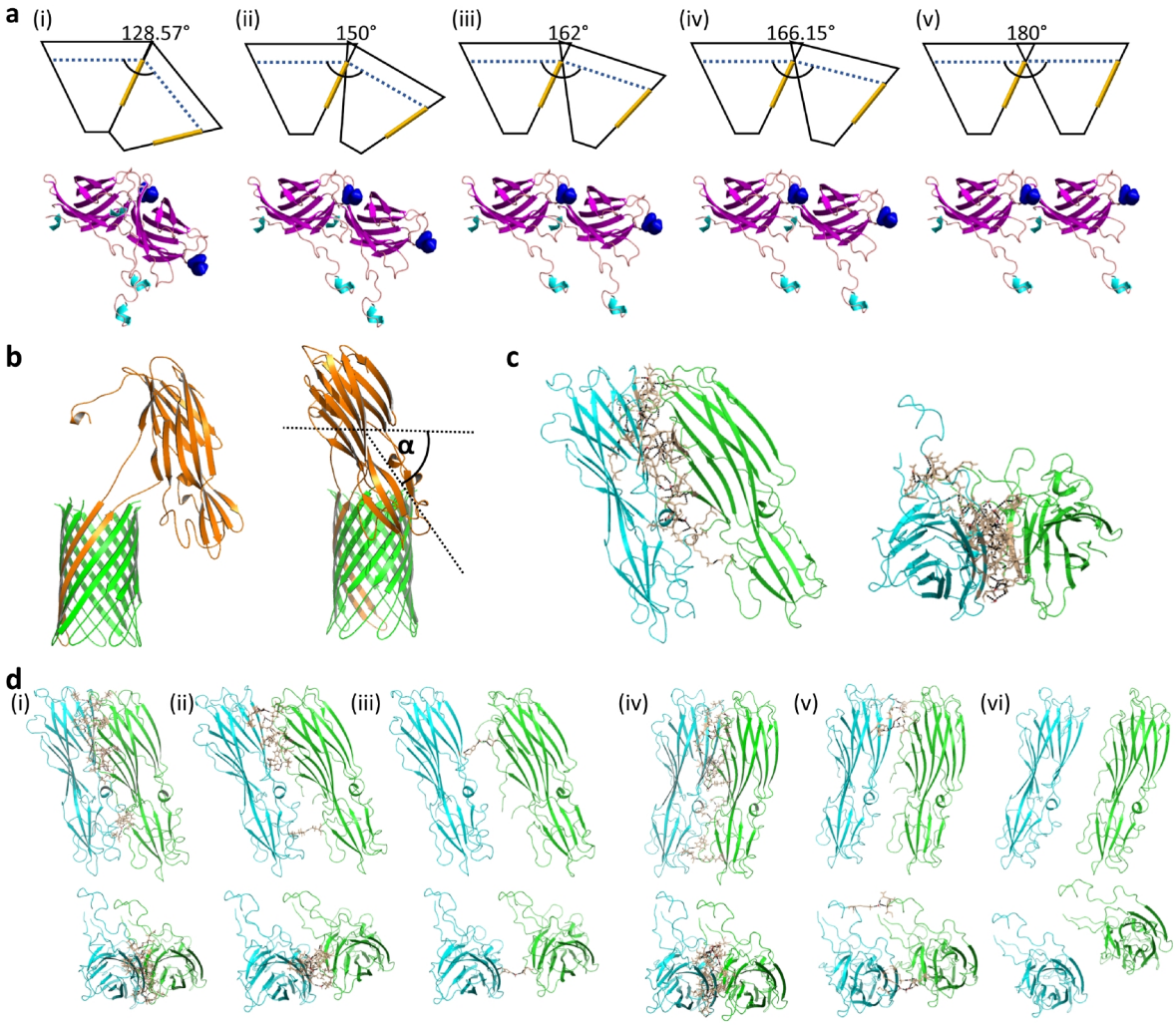

Supplementary Figure 24| Arrangement of the cap domain for pores with expanded diameters. a, Geometrical (top) and molecular (bottom) schematic representation of the monomer arrangement at different separation angles for a (i) 7-, (ii) 12-, (iii) 20- and (iv) 26-mer and (v) against an infinite number of monomers. The outer position of the monomer-monomer interaction side (highlighted in orange) is considered a turning point. The molecular representation shows the β-sandwich domain and amino latch only. **b**, Alignment of a monomer within the wild-type αHL pore (PDB code: 7ahl). **c**, Non-covalent interaction between the monomers in the wild-type αHL pore (left: side view; right: top view). **d**, Side view (top) and top view (bottom) of monomer-monomer interaction within the cap domain of an icosamer along the barrel with a (i, iv) 4 aa-, (ii, v) 6 aa-, and (iii, vi) 8 aa-offset based on the values given in Table S1. (i-iii) represent the cap domain at a rotation angle α as in the heptameric pore, whereas (iv-vi) are rotated by the same angle as the β-hairpins within the barrel.

In addition to subunit interactions in the transmembrane domain, the inclined cap alignment of a monomer within the wild-type αHL pore gives rise to polar contacts of adjacent protomers. These are mainly between the β-sandwich domains, but also between amino latches, β-sandwich and amino latch, β-sandwich and rim domain, and between the triangle regions (Supplementary Fig. 24c). The expansion of the αHL pore with increasing number of monomers induces a gap between the monomers that theoretically leads to a decrease in monomer-monomer interactions especially in the amino latches and the inner regions of the β-sandwich domain (Supplementary Fig. 24a).

In order to predict the possible arrangement of the cap domains within an icosameric assembly, we first considered the monomer rotated by the same angle α as in the wild-type heptameric pore (Supplementary Fig. 24b). The resulting structural arrangement shows that the dimensions for a barrel with a 6 aa-offset would result in several monomeric interactions between the adjacent β-sandwich domains as well as adjacent rim domains (Supplementary Fig. 24d(ii)). A 4 aa-offset can be ignored due to an overlap of the monomers in the circular arrangement (Supplementary Fig. 24d(i)); similarly, the dimensions of an 8 aa-offset are unlikely since the large distance between the monomers would not give rise to formation of any intermolecular polar contacts (Supplementary Fig. 24d(iii)). This approach requires flexible regions, such as the triangular region, to compensate for the different alignments of the transmembrane and cap domains.

In the second approach, we considered the whole monomeric structure fixed as it was reported to be in the αHL heptamer. Thus, the alignment of the β-hairpins within the transmembrane pore would result in rotation of the cap domain by the same angle α (considering the original position at α = -38.05° for a 0 aa-offset). Here, the resulting structures also indicate a 6 aa-offset as the most likely arrangement for formation of molecular interactions; whereas the 4 aa-offset would result in overlapping monomers (Supplementary Fig. 24d(iv-vi)). A lower number of polar contacts were found for the rotated cap in these structures. A further structural arrangement towards a smaller circular shape of the cap domains might result in an increasing number of interactions between the protomers. However, polar contacts will occur between different residues with changing stoichiometry of the protein pores.

Greater insights into the formation and stability of the monomeric assembly can be expected from molecular dynamic simulations. However, the development of *in situ* methods for the prediction of structures of multimeric complexes is still ongoing (10); thus, more detailed investigation of the monomeric assembly, beyond the symmetric docking used here, is as yet not feasible.

Section 9| Insertion mechanism of the hybrid pore constructs

We surmise that the DNA/αHL hybrid constructs insert into the bilayer according to the proposed model for heptameric αHL pore formation (11-13). This model involves the formation of a prepore[2] on the lipid bilayer, and the subsequent formation of a β-barrel due to release of the glycine-rich loops triggered by inter-protomer- and protein-membrane-interaction. While the oligomerization of the pre-pore is likely to be introduced in solution by the arrangement along the DNA nanostructure, we hypothesize that the second step representing the prepore-to-pore transition can be also used to describe the insertion of the DNA/αHL hybrid pores.

In the case of hybrid pores with a β-barrel that is shorter than the length of the lipid bilayer, the β-barrel only spans about half of the bilayer. Alternatively, it is possible that the DNA/αHL hybrid constructs with shorter β-barrels locally distort bilayers by toroidal pore formation, as seen for truncated αHL pores (14).

[2] The term prepore used in this model for the heptameric αHL pore formation differs from the term "pre-pore" we used to define the first stage of the insertion conductance profile of the hybrid pore in our manuscript. The latter might be affected by possible pre-pore binding, interprotomer or lipid rearrangements.

Supplementary Materials

HPLC-purified DNA oligonucleotides were purchased from biomers.net as lyophilized powder. Unmodified and phosphorylated oligonucleotides were dissolved in ddH_2O at a concentration of 100 μM. The amino-modified oligonucleotide (ssDNA tail') was resuspended in 0.1 M phosphate buffer (pH 7.85) to a concentration of 800 μM. The lipid used in this study was 1,2-diphytanoyl-sn-glycero-3-phosphocholine (DPhPC) (Avanti Polar Lipids). The lipid was dissolved in hexadecane (Sigma-Aldrich).

Ammonium acetate, calcium chloride, ethylenediaminetetraacetic acid, imidazole, InstantBlue™ - Protein Stain for PAGE, magnesium acetate, magnesium chloride, pentane, potassium chloride, tris(2-carboxyethyl)phosphine (TCEP), sodium chloride, sodium phosphate dibasic, sodium phosphate monobasic, sodium dodecyl sulfate (SDS), Tris-acetate-EDTA (TAE) buffer, glycine, triton X-100 and Trizma base were all purchased from Sigma-Aldrich. Any kD™ Mini-Protean® TGX precast protein gel and Precision Plus Protein™ Standards were from Bio-Rad Laboratories, Inc. λ-DNA, Quick Ligation Reaction Buffer and Quick T4 DNA Ligase were procured from New England Biolabs Inc. N-ε-maleimidocaproyl-oxysulfosuccinimide ester (Sulfo-EMCS) and SYBR Gold Nucleic Acid Gel Stain were obtained from Thermo Fisher Scientific. Poly-methylmethacrylate (PMMA 495 a5) was purchased from MicroChem. All chemicals were used as received without further purification.

Potassium chloride buffers (0.05 – 1.5 M KCl, 25 mM Tris, 50 - 400 μM EDTA, pH 7.99 - 8.0), and TEM buffer, were prepared and membrane-filtered (0.2 μm cellulose acetate, Nalgene) prior to use.

References

1. Harshman, S., Sugg, N. and Cassidy, P. (1988) Preparation and purification of staphylococcal α-toxin. *Methods Enzymol.*, **165**, 3–7.
2. Menestrina, G. (1986) Ionic channels formed by Staphylococcus aureus alpha-toxin: voltage-dependent inhibition by divalent and trivalent cations. *J. Membr. Biol.*, **90**, 177–190.
3. Murzin, A. G., Lesk, A. M. and Chothia, C. (1994) Principles determining the structure of b-sheet barrels in proteins I. A theoretical analysis. *J. Mol. Biol.*, **236**, 1369–1381.
4. Murzin, A. G., Lesk, A. M. and Chothia, C. (1994) Principles determining the structure of b-sheet barrels in proteins II. The observed structures. *J. Mol. Biol.*, **236**, 1382–1400.
5. Liu, W.-M. (1998) Shear numbers of protein β-barrels: definition refinements and statistics. *Journal of Molecular Biology*, **275**, 541–545.
6. Butler, T. Z., Pavlenok, M., Derrington, I. M., Niederweis, M. and Gundlach, J. H. (2008) Single-molecule DNA detection with an engineered MspA protein nanopore. *Proc. Natl. Acad. Sci. U.S.A.*, **105**, 20647-20652.
7. Song, L. Z., Hobaugh, M. R., Shustak, C., Cheley, S., Bayley, H. and Gouaux, J. E. (1996) Structure of staphylococcal alpha-hemolysin, a heptameric transmembrane pore. *Science*, **274**, 1859–1866.
8. Kowalczyk, S. W., Grosberg, A. Y., Rabin, Y. and Dekker, C. (2011) Modeling the conductance and DNA blockade of solid-state nanopores. *Nanotechnology*, **22**, 315101.
9. Pratt, K. W., Koch, W. F., Wu, Y. C. and Berezansky, P. A. (2001) Molality-based primary standards of electrolytic conductivity (IUPAC Technical Report). *Pure Appl. Chem.*, **73**, 1783–1793.
10. Degiacomi, M. T. and Peraro, M. D. (2013) Macromolecular Symmetric Assembly Prediction using Swarm Intellicence Dynamic Modeling. *Structure*, **2**, 1097–1106.
11. Yamashita, D., Sugawara, T., Takeshita, M., Kaneko, J., Kamio, Y., Tanaka, I., Tanaka, Y. and Yao, M. (2014) Molecular basis of transmembrane beta-barrel formation of staphylococcal pore-forming toxins. *Nat. Commun.*, **5**, 4897.
12. Walker, B., Krishnasastry, M., Zorn, L. and Bayley, H. (1992) Assembly of the oligomeric membrane pore formed by staphylococcal alpha-hemolysin examined by truncation mutagenesis. *J. Biol. Chem.*, **267**, 21782–21786.
13. Walker, B., Braha, O., Cheley, S. and Bayley, H. (1995) An intermediate in the assembly of a pore-forming protein trapped with a genetically-engineered switch. *Chem. Biol.*, **2**, 99–105.
14. Stoddart, D., Ayub, M., Höfler, L., Raychaudhuri, P., Klingelhoefer, J. W., Maglia, G., Heron, A. and Bayley, H. (2014) Functional truncated membrane pores. *Proc. Natl. Acad. Sci. U.S.A.,* **111**, 2425–2430.